JGR Space Physics

RESEARCH ARTICLE
10.1029/2019JA027345

High-Resolution Optical Observations of Neutral Heating Associated With the Electrodynamics of an Auroral Arc

D. J. Price[1], D. K. Whiter[1], J. M. Chadney[1], and B. S. Lanchester[1]

[1]School of Physics and Astronomy, University of Southampton, Hampshire, UK

Key Points:
- Development of a new observing technique allows for the measurement of neutral temperature profiles during auroral events at an unprecedented temporal resolution
- A case study of a morning sector auroral arc over Svalbard reveals a region of significant Joule heating on its poleward edge
- Evidence of a separate Ohmic heating signature embedded within the arc and associated with strong field aligned currents

Supporting Information:
- Supporting Information S1

Correspondence to:
D. Price,
D.J.Price@soton.ac.uk

Citation:
Price, D. J., Whiter, D. K., Chadney, J. M., & Lanchester, B. S. (2019). High-resolution optical observations of neutral heating associated with the electrodynamics of an auroral arc. *Journal of Geophysical Research: Space Physics*, *124*. https://doi.org/10.1029/2019JA027345

Received 27 AUG 2019
Accepted 23 OCT 2019
Accepted article online 6 NOV 2019

Abstract We present results that indicate the existence of two distinct neutral heating processes associated with a discrete auroral arc over Svalbard. Within the order of seconds, the thermospheric temperature profile displays a significant response to the arc on spatial scales smaller than 10 km. It is suggested that both heating signatures are associated with the electrodynamic system responsible for the formation of the arc. Pedersen currents produce a temperature increase of approximately 100 K, observed at altitudes between 80 and 160 kilometres, directly adjacent to the arc structure and on its poleward edge only. In contrast, field-aligned currents produce a variable temperature increase, of approximately 50 K, which is observed within the arc itself and constrained to a narrow altitude range between 90 and 110 km. By utilizing a range of observations and new analysis methods we are able to measure the atmospheric neutral temperature profile, over auroral altitudes, at unprecedented temporal and spatial scales. The High Throughput Imaging Echelle Spectrograph records high-resolution emission spectra of the aurora, which are then fitted with synthetic N_2 spectra, generated with modeled N_2 volume emission rate profiles and a library of trial temperature profiles. The N_2 volume emission rate profiles are retrieved from the Southampton ionospheric model using precipitating particle energies and fluxes obtained from Auroral Structure and Kinetics and the EISCAT Svalbard Radar. The application of this technique allows us to produce a time series of neutral temperature profiles and measure the localized heating of the neutral atmosphere resulting from the electrodynamics of the arc.

1. Introduction

It has long been understood that the auroral displays present at high latitudes are a consequence of complex magnetosphere-ionosphere interactions that are governed by a system of extensive magnetic field-aligned currents (FAC; Iijima & Potemra, 1976, 1978). The general picture is of two large (oval scale) rings of FAC sheets, separated into "Region 1" currents at high latitudes (~66–76°) and "Region 2" currents at lower latitudes (~62–72°), with some crossover depending on the magnetic local time. They display opposite polarities in the dusk and dawn sectors of the polar cap and are closed through the ionosphere via meridional Pedersen currents. A second ionospheric current system is found in the form of significant Hall currents flowing both sunward, across the center of the polar cap, and antisunward, along the oval in both the morning and evening sectors. The latter of these Hall currents are known as the westward and eastward auroral electrojets, respectively (Boström, 1964). This overarching system is complicated by a variety of smaller-scale currents, embedded within the larger system, which are presumed to be linked to various suboval auroral structures. FAC systems in the auroral region have been observed to have a large range of scales, between ~500 km and a few hundreds of meters (Lühr & Warnecke, 1994; Stasiewicz & Potemra, 1998; Wu et al., 2017), suggesting that the Regions 1 and 2 currents are in fact composed of the sum of both upward and downward smaller-scale FACs. Simulations have shown that the formation of these small-scale currents is driven by Alfvén waves propagating and reflecting in the ionosphere (Zhu et al., 2001).

Perhaps the simplest suboval auroral structure is the auroral arc, an east-west aligned structure with variable thickness (Partamies et al., 2010), that is relatively steady on time scales between 10 and 100 s (Marghitu, 2012). The electrodynamic structure of auroral arcs has been extensively studied for many years despite the difficulties inherent in measuring the associated electric fields, conductivities, and currents at sufficient temporal and spatial resolution. Marklund (1984) developed an arc classification scheme based on the relative contribution of the polarization electric field and the Birkeland currents to the electrodynamic system. He distinguished three main categories of arc: polarization arcs, Birkeland current arcs, and

combination arcs (a transitional case) by determining which regime provided the dominant source of current continuity in the ionosphere. A common, but not universal, feature observed in case studies of auroral arcs is an enhanced electric field perpendicular to the arc alignment (e.g., north or south directed). The electric fields are observed adjacent to the visual arc structure but are often reported to be asymmetric; they are generally found to be on the equatorward edge of the arc in the evening sector and the poleward edge in the morning sector, a configuration that is thought to relate to the direction of the background ionospheric convection field (Aikio et al., 1993; Marklund et al., 1982; Opgenoorth et al., 1990; Timofeev et al., 1987). Timofeev et al. (1987) associated with the often observed "radar arc" with a Hall current arising adjacent to the arc structure due to the presence of the perpendicular arc-associated electric field (AAEF) and Aikio et al. (1993) concluded that the enhanced AAEF observed by them and many others is driven by the electrodynamical system of the arc. Arcs such as these would be associated with the Birkeland or combination arc classifications outlined in Marklund (1984), meaning that the FAC and the resulting ionospheric Pedersen currents play a significant role in maintaining the current continuity in the ionosphere.

Large-scale ionospheric Joule heating is well understood to be a significant factor in the dissipation of the total solar wind energy that enters the magnetosphere, which has been estimated to be of the order of 10^{12} W (Rodger et al., 2001). Sharber et al. (1998) report that, for a particular storm, the Northern Hemispheric Joule heating rate can be as high as 290 GW, whereas the corresponding power deposited via direct particle participation is ~50 GW. This result, among others, suggests that Joule heating is responsible for ~55–65% of the total energy budget of the magnetosphere-ionosphere system (Fujii et al., 1999; Østgaard et al., 2002).

The conventional expression for the rate of local Joule heating is given by

$$Q_j(h) = \sigma_p(h)[\mathbf{E}_\perp + \mathbf{u}(h) \times \mathbf{B}]^2 \tag{1}$$

where $\sigma_p(h)$ is the Pedersen conductivity, $\mathbf{E}_\perp$ is the convection electric field, $\mathbf{u}(h)$ is the ionospheric neutral wind velocity, $\mathbf{B}$ is the ambient geomagnetic field, and h is the altitude. Since it is difficult to determine the large-scale ionospheric electric field and the corresponding Pedersen conductivities, attempts to quantify the global Joule heating rate typically rely on a number of simplifying assumptions. Popular approaches can be separated into two main categories: either identifying and utilizing relevant magnetic indices as proxies for the global Joule heating rate (Chun et al., 1999, 2002; Kosch & Nielsen, 1995) or solving a height-integrated version of equation (1), in which the neutral wind speed is assumed to be negligible (Kosch et al., 2011). Furthermore, another common assumption required in any estimate of global Joule heating rate is that the ionospheric electric field is relatively smooth, both temporally and spatially, and therefore values are usually averaged and produced on time scales of approximately an hour (Kosch & Nielsen, 1995). This averaging of the electric field in time and space has been shown to result in considerable underestimations of the total Joule heating, sometimes as high as 65% (Rodger et al., 2001). Codrescu et al. (1995) presented incoherent scatter radar measurements of the highly varying nature of the high-latitude electric field and argued that the square of the average field, as is often used, is substantially smaller than the average of the squared electric field, which they suggest leads to an underestimation of the total Joule heating of ~50%.

Multiple radar and rocket studies of discrete auroral arcs have reported strong localized electric fields adjacent to the boundaries of auroral arcs (Aikio et al., 1993; Lanchester et al., 1996, 1998; Marklund et al., 1982), and often these observations are linked with simultaneous observations of enhanced ion or electron temperatures (Han et al., 2019; Kosch et al., 2011; Lanchester et al., 2001; Opgenoorth et al., 1990). Furthermore, Kiene et al. (2019) recently reported significant spatial structure in ion temperatures and Joule heating rates during periods of enhanced magnetic activity. These results all suggest the presence of small-scale and highly variable heating mechanisms associated with auroral activity. Understanding the effects of these small-scale variations in the global picture of the high-latitude ionosphere is vital in gaining a better understanding of the large-scale consequences of the ionosphere-magnetosphere system.

During periods of high-energy particle precipitation associated with bright auroral arcs, the majority of the energy is deposited into the E region of the ionosphere (~90–150 km; Kaila, 1989, and references therein). For more quiescent periods it is a reasonable approximation that the ion temperature is equivalent to the neutral temperature (Nozawa et al., 2006), but for periods of intense electric field enhancements (>100 mV/m) it has been shown that the ion temperature can exceed that of the modeled neutral temperatures by upward of 300 K (Maeda et al., 2005). The majority of local, arc-associated Joule-heating observations rely on ground-based radar measurements of enhanced ion temperatures in the vicinity of an

optical arc. However, the corresponding neutral temperatures are much more difficult to measure remotely, usually requiring an in situ rocket campaign and are instead often inferred using atmospheric models. As a result of these limitations, the response of atmospheric neutral temperatures to the presence of the electrodynamics of auroral structures is not well understood. Kurihara et al. (2009) recorded N_2 rotational temperatures from an instrument on board a Japanese-sounding rocket during an auroral event; their measurements showed a uniform temperature enhancement of 70–140 K in the 110–140 km altitude range, in which they used the MSISE-90 atmospheric model as the baseline. They attributed the majority of the heating to a "passive energy deposition" rate, which they describe as an alternative to Joule heating wherein the neutral wind effect is neglected and reported a peak heating rate of 0.5 $\mu W/m^{-3}$ at 120 km. Inferring atmospheric neutral temperatures from N_2 rotational spectra is an often employed diagnostic tool (Jokiaho et al., 2008) but has previously been limited to measurements of altitude averaged emission profiles, or one-time rocket trajectories, making it hard to infer the presence of any local heating (Henriksen et al., 1987). We present a novel technique for the measurement of *E* region neutral temperature altitude profiles at unprecedented temporal and spatial resolutions, allowing for further investigation of the thermospheric response to the arc-associated electrodynamic system, specifically neutral temperature changes.

2. Observations

The observations used in this work were made near Longyearbyen, Svalbard (78.15°N, 16.03°E), during a fieldwork campaign in January 2017. A very bright auroral arc observed during the expansion phase of a magnetic substorm on 27 January is the subject of this paper. At this time Svalbard was located in the near-midnight sector of the polar cap just eastward of the convection reversal. All-sky images taken from the Kjell Henriksen Observatory (KHO) show a structured, east-west aligned auroral arc spanning the sky just south of the magnetic zenith. At 20:50:40 UT this extremely bright and dynamic arc begins expanding northward, and its poleward edge passes into the magnetic zenith. In the following 90 s a large fold develops in the center of the all-sky field of view, moving the arc structure northward until it has completely passed over the magnetic zenith. During this interval the arc was observed by a number of instruments introduced in detail below.

2.1. HiTIES

The HiTIES (High Throughput Imaging Echelle Spectrograph) instrument is fitted with a multipanel mosaic filter, which allows for the simultaneous spectral imaging of a number of noncontiguous wavelength regions at high spectral resolution. HiTIES is part of the Spectrographic Imaging Facility (SIF) and is hosted at KHO. Emissions from the aurora are observed via a north-south aligned slit (centered approximately on local magnetic zenith) with an angular size of 8° along the slit and 0.05° across it. Incoming light is dispersed into its components via an echelle grating onto an Electron Multiplying Charge Coupled Device, which records at a time resolution of 0.5 s. In order to ensure a high signal-to-noise ratio the spectra are typically postintegrated in time to ~2 min resolution. However, during periods of extremely bright emission the resolution can be reduced to the order of seconds. The mosaic panel used in this work has a wavelength range of 728–740 nm and a resolution of 0.12 nm. During times of high-energy particle precipitation, the dominant auroral emission in this wavelength region comes from vibrational transitions of the N_2 1PG band ($B^3\Pi$ - $A^3\Sigma$). Other emissions include the OH(8–3) band (airglow), two auroral O^+ doublets at wavelengths $\lambda = 732.01$ and 731.90 nm and $\lambda = 733.08$ and 732.97 nm (Whiter et al., 2014), and a small contribution from O_2^+ 1N auroral emission ($b^4\Sigma_g^-$ - $a^4\Pi_u$).

2.2. ASK

The ASK instrument (Auroral Structure and Kinetics) is a narrow angle optical imager consisting of three cameras with identical fields of view, each aligned with the magnetic zenith. Each camera records at 32 frames per second and is fitted with a spectral filter centered on a different emission of interest. ASK has a field of view of 6.2° by 6.2° which corresponds to a length scale of approximately 10 km at auroral emission altitudes. These features allow for the investigation of the rapidly evolving and small-scale filamentary structure commonly observed within the larger scale structure of auroral displays (Ashrafi, 2007; Dahlgren et al., 2008; Sandahl et al., 2008). The central wavelengths and full width half maximums of the filters in use on ASK 1 and 3 are shown in Table 1. This study will use the emissions present in ASK 1 (N_2) and ASK 3 (O); N_2 emission is sensitive to high-energy particle precipitation and O emission to a mix of high- and low-energy precipitation. The ratio of emission brightness between these two cameras, integrated in a region

Table 1
Table of Properties of the Relevant ASK Cameras

Camera	Central wavelength (nm)	FWHM (nm)	Emission
ASK 1	673.0	15.0	N_2
ASK 3	777.4	1.3	O

Note. ASK = Auroral Structure and Kinetics; FWHM = full width at half maximum.

surrounding the magnetic zenith, thus allows for estimates of the energy and flux of precipitation that corresponds to the different discrete auroral structures within scale sizes of 100 m and at the time resolution of the images (Lanchester et al., 2009). The ASK instrument is located at the EISCAT Svalbard Radar (ESR) building (78.15°N, 16.03°E), separated from KHO and HiTIES by approximately 500 m. ASK is absolute intensity-calibrated using cataloged reference stars.

2.3. EISCAT

The EISCAT Svalbard Radar is an ultrahigh frequency (500 MHz) incoherent scatter radar consisting of a fixed field-aligned 42 m dish and a steerable 32 m dish. During operational hours of the January 2017 campaign the 32 m dish was aligned with the local magnetic zenith and the radar experiment "arc_slice" was run, utilizing both antennas. This experiment contains a 64 bit alternating code experiment that allows EISCAT to return power profiles at 0.5 s resolution at altitude steps of 0.9 km between 85 and 481 km. The returned power spectra are postintegrated to 5.0 s resolution and fitted to give electron temperatures, ion temperatures and electron densities.

3. Methods and Data

As discussed in section 1, measuring rotational and vibrational temperatures by comparing observed emission spectra with those produced via a model is a well-established and commonly used technique. However, in the context of estimating neutral temperatures with ground-based observations of auroral N_2 emissions, a number of difficulties present themselves. Fitting a synthetic spectra that represents a single fixed rotational temperature is a reasonable method provided that two key assumptions can be relied upon. These are the following:

1. The lower rotational and vibrational states have undergone enough collisions to be in local thermodynamic equilibrium with the neutral atmosphere.
2. The emitting species occupies a sufficiently thin atmospheric layer such that its temperature is uniform and unaffected by the local atmospheric temperature profile.

The first of these assumptions is generally well accepted; the N_2 rotational temperature is expected to be approximately equal to the neutral temperature in the *E* region. The equilibrium between rotational and translational degrees of freedom for N_2 is maintained by a high-collision frequency in the lower thermosphere (Kurihara et al., 2006). However, the second assumption is likely not valid when considering emission from auroral N_2. Modeling shows that during particle precipitation events the spectrum of precipitation energies leads to large altitude extent at which there is considerable N_2 emission (Lanchester et al., 2009). Consequently, due to gradients in the atmospheric temperature profile over the same altitude range, ex situ observations (e.g., ground-based) often contain emission from a large range of N_2 temperatures. To account for the breakdown of assumption 2, we have developed a new technique that allows for measurements of the neutral temperature profile at the altitudes at which the N_2 volume emission rate is significant. The method can be separated into the following four steps, each of which is discussed in detail below:

1. Determine the particle precipitation energy and flux associated with the optical emission using the ASK instrument.
2. Retrieve an estimate of the N_2 volume emission rate profile as a function of time, by using the energy and flux from Step 1 as an input to an ion chemistry and electron transport model.
3. Generate a library of synthetic N_2 volume emission spectra by combining a range of trial temperature profiles and the modeled N_2 volume emission rate profile.
4. Fit the synthetic N_2 emission spectra to those observed by the HiTIES instrument during the event to determine a time series of best fit neutral temperature profiles.

3.1. Particle Precipitation Energy and Flux

Determining the distribution of the particle precipitation energies within auroral structures is a powerful tool for developing an initial understanding of the mechanisms involved in producing the vast variety of observed auroral morphology. Accelerated electrons descend magnetic field lines and collide with atmospheric constituents. The resulting emission intensities are principally determined by the altitude range at which the secondary electron energy is deposited, which in turn is reliant on the primary precipitation

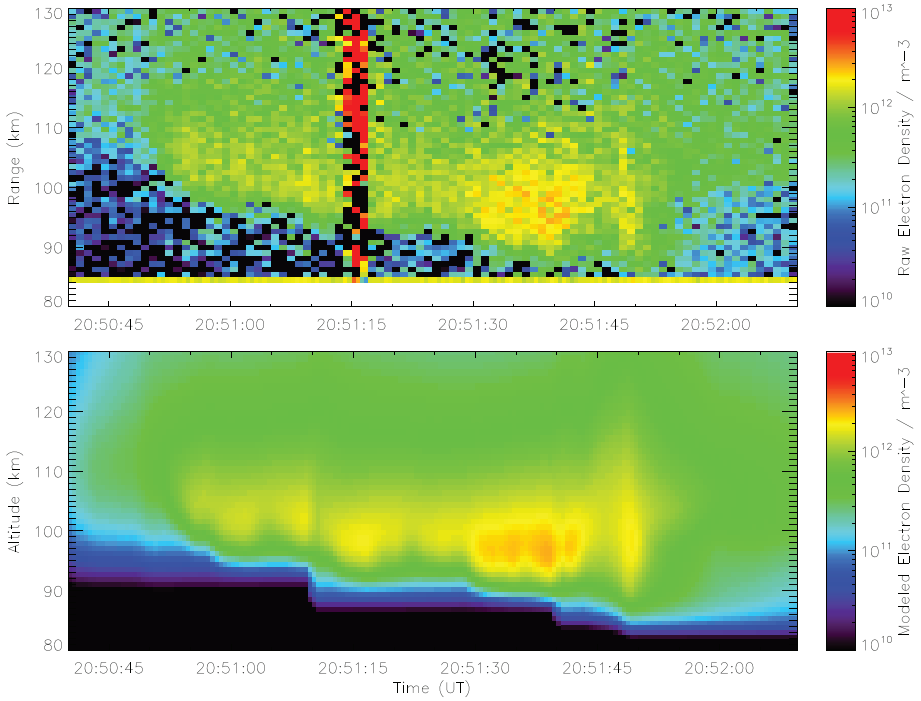

Figure 1. Comparison between the observed raw electron density from the EISCAT Svalbard Radar (top panel) and the corresponding modeled electron density from the University of Southampton ion chemistry and electron transport model (bottom panel). The large red artifact visible in the ESR power profiles is a result of a poor fit in the analysis software and was ignored in the analysis.

energy (Lummerzheim & Lilensten, 1994). The ASK instrument is well equipped to exploit this relationship by comparing the emission intensities observed in each of its cameras. ASK1 (673 nm) is centered on N_2 emission that originates from two N_2 1P vibrational band transitions (4,1) and (5,2). N_2 density is concentrated at lower altitudes (~100 km) and thus this emission is responsive to high-energy precipitation. ASK3 (777.4 nm) isolates atomic oxygen emission arising from the 3s ^{5}S – 3p ^{5}P multiplet, which is sensitive to a mixture of low and high energies. By measuring the ratio between these two emissions it is possible to infer the precipitation energies and fluxes. We can retrieve this information at the time resolution of the ASK instrument (32 Hz; Dahlgren et al., 2008; Lanchester et al., 2009).

3.2. N_2 Volume Emission Profile

In order to measure neutral temperatures with N_2 emission we first need a valid estimation of both the shape and time evolution of the N_2 volume emission rate profile. The precipitation energy and flux from ASK, as well as activity parameters for the night in question (AP, *F*10.7, and 81-day average *F*10.7), are used as inputs into the Southampton electron transport and ion chemistry model (Lanchester et al., 1994; Palmer, 1995). The model solves 1-D field-aligned electron transport and coupled time-dependent continuity equations for neutral and ion species over a range between 80 and 500 km. The result is the modeled atmospheric response to energetic particle precipitation, including volume emission rates and densities of key constituents, as a function of time. The output of the model is verified by comparing the modeled electron densities with those measured by the ESR during the course of the event. Figure 1 displays this comparison at half second resolution and shows a good agreement between the two data sets. The model successfully reproduces the descent of the electron density peak from ~105 km, at the arrival of the aurora in the radar beam (20:50:50 UT), to as low as 95 km during the period of most intense emission (20:51:30–20:51:52 UT). Fluctuations in electron density on time scales of the order of seconds are also correctly reproduced, most notably at 20:51:45 UT when a drop-off and subsequent resurgence in electron density is seen. This result gives confidence in the N_2 volume emission rate profiles retrieved from the model.

3.3. Synthetic N_2 1P Emission Spectra

The transitions between the two states of N_2 that contribute to the 1P band ($B^3\Pi$ - $A^3\Sigma$) are well documented, and the brightness contributions of the various energy levels can be calculated given the appropriate molecular constants (Jokiaho et al., 2008). Molecular constants for the modeling of synthetic N_2 1P emission spectra

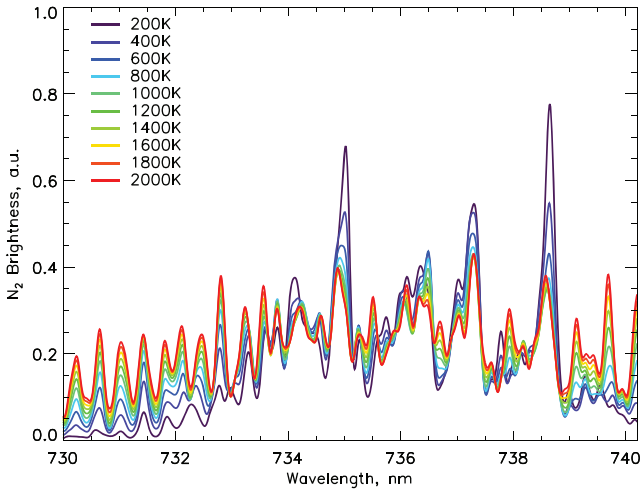

Figure 2. N_2 synthetic 1P emission spectra in the wavelength region of interest, for a range of rotational temperatures.

can be found in Roux and Michaud (1990). Figure 2 displays a selection of these synthetic emission spectra, convolved onto the HiTIES wavelength grid, for a range of temperatures. A library of synthetic N_2 1P emission spectra, over the wavelength range of the chosen HiTIES panel (728–740 nm), has been produced for a set of possible atmospheric temperature profiles. These temperature profiles were generated in the following way. A temperature profile for the time and day in question was generated using the NRLMSISE–00 empirical model of the atmosphere (Picone et al., 2002). Then a uniform random sample of temperatures and altitudes, centered around the NRLMSISE–00 defined mesopause, were chosen as initial conditions for a series of random walks in both increasing and decreasing altitude, with minimum and maximum values at 80 and 200 km, respectively. The temperature gradient during this random walk process was weakly constrained to favor a positive gradient above the mesopause, and vice versa below the mesopause. The result is a collection of trial temperature profiles, which provide significant coverage of a range of potential temperatures and gradients within the chosen altitude range.

The complementary library of synthetic N_2 1P spectra can now be generated; these spectra each represent an entire temperature profile (between 80 and 200 km) instead of a single rotational temperature, such as those displayed in Figure 2. For each N_2 volume emission rate profile and trial temperature profile there are corresponding values of temperature and volume emission rate at every altitude step. A temperature profile can therefore be represented by a temperature histogram with bins that contain the total N_2 volume emission rate found at that temperature, over the entire altitude range. Consequently, to build a synthetic spectrum from a temperature profile we integrate the components of each of the temperature bins in the associated histogram. The central temperature of each bin is used to generate an individual synthetic N_2 line spectra for that rotational temperature. These line spectra are then summed into a total line spectra, weighted according to the amount of volume emission in each bin. By summing across all temperatures we build up the total contribution to the synthetic spectra from the entire altitude range. The resultant synthetic line spectra are convolved with a Gaussian instrument function, with a full width half maximum of 0.06 nm, to acquire a matching theoretical convolved brightness on the same wavelength grid as observations from HiTIES. The same method is applied to generate the synthetic O_2^+ spectra that are used in the fitting process (section 3.4); however, the total contribution from this band is significantly less than the N_2 1P emission.

3.4. Spectral Fitting

During the 90 s in which the arc is passing through the magnetic zenith its brightness varies significantly. HiTIES spectra can therefore be integrated for a varying amount of time, depending on the emission brightness, before an acceptable signal-to-noise ratio is reached. The result is displayed in Figure 4 (bottom panel) which shows the ASK1 (673 nm) brightness and the duration of each HiTIES integration period. The N_2 volume emission rate profiles from the ionospheric model (at 0.5 s resolution) are also integrated to line up with these periods. The result is therefore a time series of 29 N_2 volume emission rate profiles and their corresponding observed emission spectra, covering the time the auroral emission is in the zenith. The final step is to find the temporal variation of the best fit temperature profile for the duration of the auroral event. This is done by fitting the synthetic spectra, and thus the corresponding temperature profiles, to each time-integrated HiTIES spectrum. We have developed a fitting routine which allows us to determine the intensities of the relevant component emissions including which synthetic N_2 spectrum best matches the corresponding observed spectrum. We apply a least squares residual fit that is composed of five separate components that are present in the relevant HiTIES panel: the auroral N_2 1P(5–3) band emission, auroral O_2^+ (0–3) band emission, six OH(8–3) emission lines, two auroral O^+ doublets (four lines total), and a constant background. The free parameters for the auroral band emissions are the peak brightness of the emission and the magnitude of water vapor absorption (Chadney et al., 2017). An example fit containing these components is displayed in Figure 3. The shape of each synthetic spectrum is determined via the integration method described in section 3.3 and as a result is unique to each histogram and volume emission profile. The

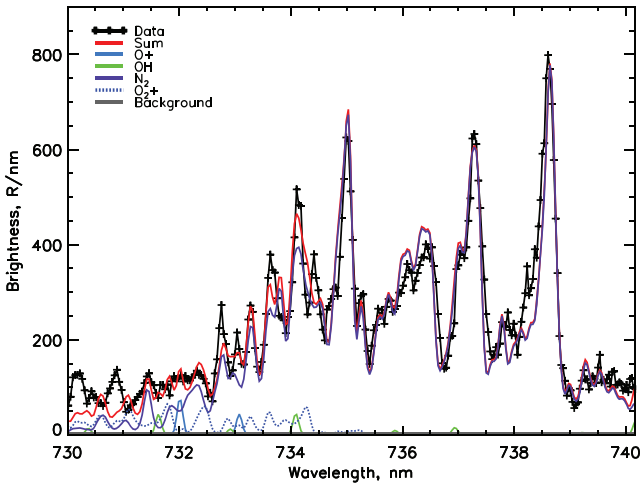

Figure 3. Example fit of a HiTIES emission spectra during a period of bright N_2 emission.

least squares residual error for each temperature histogram is used to determine the set of trial histograms that best reproduce the observed emission spectrum.

The fitting process is separated into two steps. First, 1,000 temperature profiles are generated using the method described in section 3.3, across a large range of potential temperatures (50–2200 K) at all altitudes (80–200 K). This number of initial temperature profiles was found to strike an appropriate balance between sufficient variety in candidate profiles while also reducing unnecessary computational expense. Each temperature profile in this set is converted to its corresponding histogram, used in the fitting process and assigned an error. The errors for each histogram are sorted from low to high, and the lowest 15.8% of the total population are selected. Next, we define a new range of allowed temperatures at each altitude step, using the minimum and maximum temperatures covered by the profiles in the selected population. We then regenerate another 1,000 temperature profiles, under these new boundary conditions, and run the fitting process on the corresponding histograms a second time—obtaining our final sample. This method minimizes the amount of computational time spent on temperature profiles that exhibit large errors.

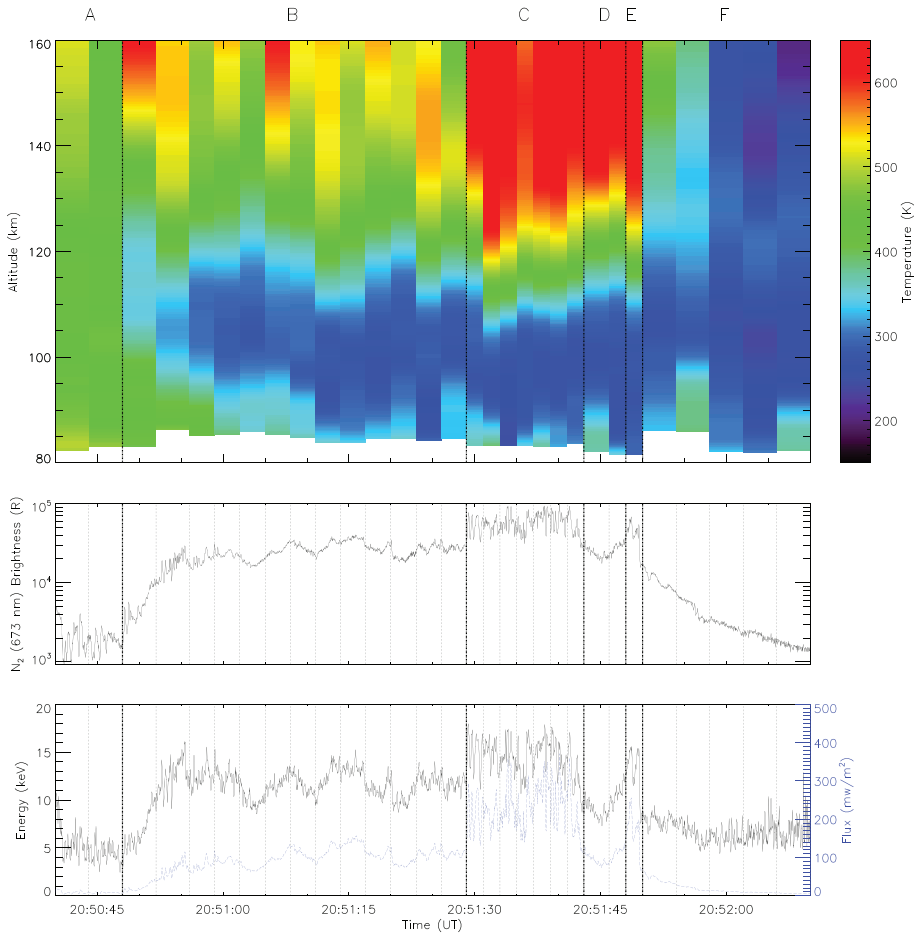

Figure 4. (top panel) Mean best fit temperature profiles. Each vertical stripe corresponds to the HiTIES integration period used to generate the observed spectrum (between 2 and 4 s). (bottom panels) The calibrated N_2 (673 nm) brightness (R) and measured particle precipitation energy and flux, respectively, as a function of time during the event. The gray vertical dashed lines correspond to the same integration periods as in the top panel, and the bold black vertical dashed lines to the time intervals labeled above the plot and discussed in section 4.

The errors corresponding to each of these histograms are approximately normally distributed and those with errors with values less than two standard deviations from the mean are chosen. Each of these histograms represents a well fitting temperature profile which is subsequently retrieved and assigned the error corresponding to the synthetic spectrum it produced. Using this selection criteria for temperature profiles we can determine an estimate of a mean temperature and uncertainty at each altitude. The fitting process for each observed spectrum takes approximately 3 hr to complete. We then repeat this analysis for each integration period (or time step) of the auroral event and build up a time series of neutral temperature profiles.

We note here that an important consideration of the following results is the shape of the N_2 volume emission profile for each corresponding neutral temperature profile. Due to the nature of the integration process, the altitude regions in which the N_2 volume emission is largest (with respect to the rest of the profile) are the same regions in which the process is most sensitive to neutral temperatures. Furthermore, since the brightness of the component spectra that build up the final spectrum is weighted by the corresponding volume emission rate, the actual value at each altitude is not important and only the shape of each of the profiles has an effect on the generated synthetic spectra.

Each temperature profile has an error which increases away from the peak of the N_2 volume emission; the contributions to the fitted synthetic spectra from the neutral temperatures in the regions of low emission are relatively small compared to those at the peak of the emission. This effect is most significant inside the auroral arc where the N_2 volume emission profile is at its narrowest in altitude and thus centered on the small altitude range at which the monoenergetic electron precipitation spectrum deposits the majority of its energy (e.g., Figure 5c). Conversely, at the edges of the arc, the N_2 volume emission profile has a wider extent in altitude, meaning that the altitude range over which the temperature has a significant effect on the shape of the synthetic spectra is equally wide (e.g., Figure 5a). A disadvantage is that the observed spectra before and after the period of brightest emission have a lower signal-to-noise ratio due the expected decrease in total emission brightness. However, we are able to constrain the neutral temperatures to good accuracy, over a large range of altitudes, in the region where it is thought the majority of the chemical and electrodynamical processes associated with the arc are taking place.

4. Results and Discussion

Figure 4 (top) shows the resulting neutral temperature profiles, each corresponding to their separate time integration periods, during the passage of the arc. The bottom panel shows the observed ASK1 (673 nm) N_2 emission brightness as a function of time. The vertical gray dashed lines indicate the HiTIES integration intervals. The event can be divided into six time intervals, indicated by the vertical black dash-dotted lines: (a) prior to the arrival of the optical arc in the field of view, HiTIES is observing the region immediately poleward of the bright emission; (b) the passage of the leading edge of the arc, consisting of dynamic structured curls in a bright diffuse background that are associated with brightness fluctuations around a relatively constant value of approximately 20 kR; (c) a period of considerably enhanced brightness related to the presence of an extremely narrow, bright, and dynamic auroral arc embedded in the main structure; (d) this narrow arc moves southward of the zenith and the N_2 brightness returns to previous levels; (e) the narrow arc moves northward again, entering the zenith for a second brief period of time before progressing northward and out of the field of view; (f) a region of diffuse aurora that gradually reduces in brightness (approaching background levels) as the large-scale structure of the arc completes its passage over the zenith. A video of the ASK field of view during these intervals is provided as supporting information.

Figure 5 displays a characteristic temperature profile and an example of the associated auroral structure seen in ASK, for each of the six time intervals defined above. The ASK images on the left-hand side show a single frame snapshot taken during each period, with the position of the HiTIES slit marked. The panels on the right show an example temperature profile retrieved during each interval, as well as the corresponding N_2 volume emission rate profile. Figure 5a shows the first measured temperature profile, taken during the time period before the bright optical arc moves into the direct line of sight of the instruments. This temperature profile displays hot (>400 K) neutral temperatures as low as 80 km in altitude. Figure 5b shows the temperature profile from when the highly dynamic poleward edge of the arc is passing through the HiTIES slit. At this time the temperature profile is cooler at the lower altitudes (<~140 km) than that observed in panel (a) but also shows a localized increase in temperature, in comparison to the temperatures observed within the

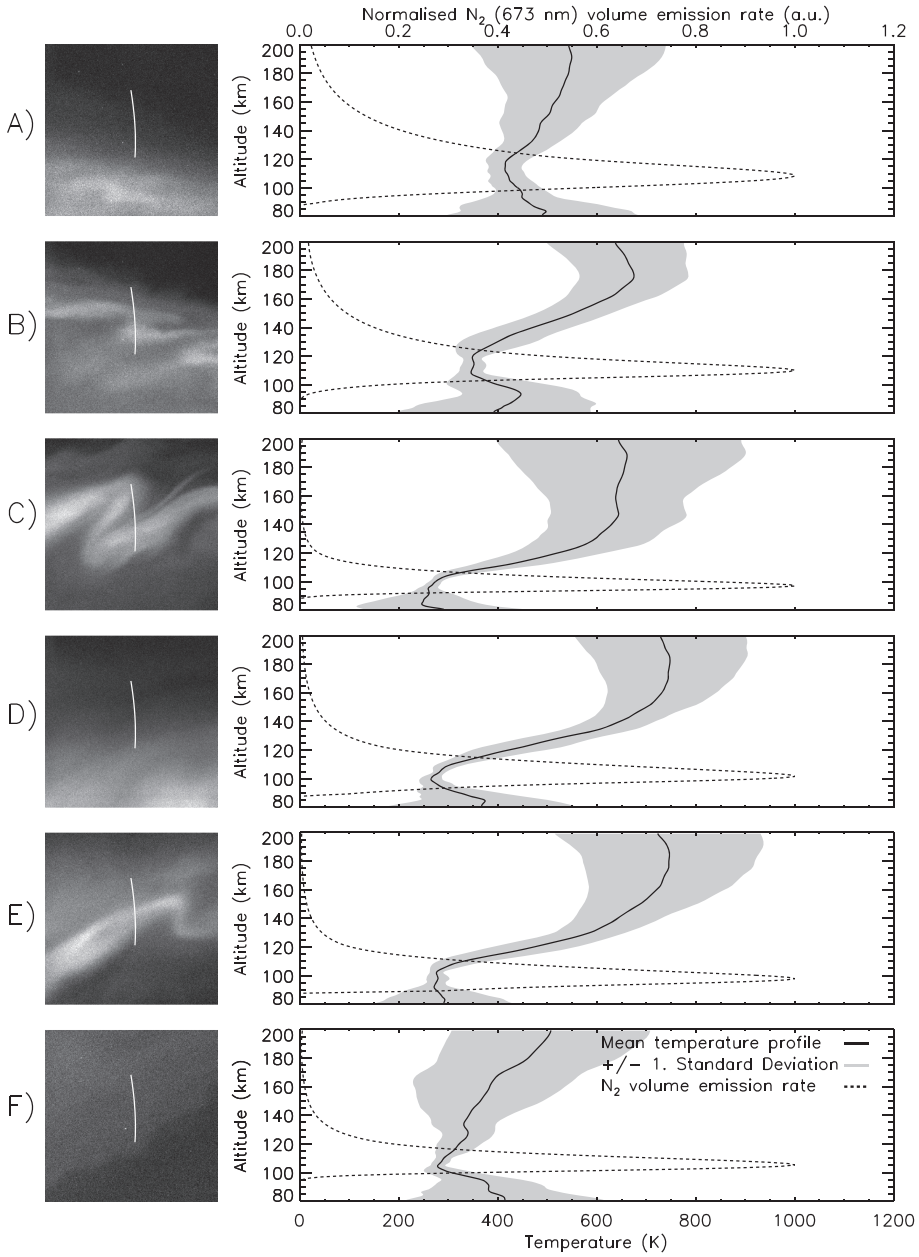

Figure 5. (a–f) Temperature profiles associated with the time periods outlined in section 4. Each profile has been selected to show the dominant features present during those times. The images on the left show a single frame snapshot of the form of the optical arc, as observed by Auroral Structure and Kinetics during those periods.

arc at later times, in the 90–110 km altitude region. Temperatures in this region show fluctuations throughout the duration of the event, but this effect is most significant in the first 10 s following the appearance of the arc in the zenith. Panel (c) is a snapshot from the region of most intense emission, when a narrow and intense arc filament, embedded in the larger arc, is within the HiTIES field of view. This is approximately 40 s after the image shown in panel (a). Here the temperatures in the altitude range between 90 and 100 km have decreased by ~150 K. Panel (d) shows a brief period of time where the intense arc has moved south of the HiTIES integration slit for approximately 6 s. This panel displays a similar shaped profile to panel (c), with slightly enhanced temperatures at the lowest altitudes. We note here that there is still significant emission within the HiTIES slit which was positioned well within the large scale optical arc structure, but due to scaling effects caused by the bright filament the ASK image appears darker in this region. Panel (e) is taken when the narrow arc is passing back through the HiTIES slit, from south to north, before moving poleward

out of the field of view, and shows a similar profile to that seen in panel (c). Panel (f) displays a temperature profile from the final interval of the passage of the arc. At this point the aurora has become much less dynamic and structured and instead appears as a diffuse emitting region that slowly moves northward. This temperature profile displays cooler temperatures than those observed at the leading edge of the arc over the majority of the altitude range.

4.1. Joule Heating on the Poleward Edge

The strong evidence of neutral heating on only the advancing poleward edge of the arc (seen in Figure 4) suggests a significant asymmetry in the underlying electrodynamics of the arc. The full formation mechanism of an optical arc and its associated electrodynamics is outlined by Aikio et al. (1993) as follows: the optical arc structure is formed via an upward FAC sheet that is carried by precipitating electrons from the magnetosphere. These precipitating electrons create a region of dramatically increased conductivity within the arc, which, in turn, can drive strong perpendicular currents and charge separation to form a polarization field. If this response is significant enough to ensure current continuity then we arrive in the Marklund (1984) polarization arc scheme. However, if the upward FAC is strong enough, or the background convection field is weak enough, such that the polarization field is not a significant factor (e.g., Birkeland arc classification) the upward FAC sheet is linked to a downward FAC sheet (carried by upward moving cold ionospheric electrons) via meridional Pedersen closing currents, ensuring current continuity in the ionosphere (Opgenoorth et al., 1990; Tsunoda et al., 1976; Zhu et al., 2001). The orientation of this current system is therefore dependent on whether the arc is observed in the evening sector (northward convection field) or morning sector (southward convection field), with equatorward and poleward connecting currents found in each respectively (Timofeev et al., 1987). In the sector close to midnight the zonal component of the convection field can be significant and this simple picture should be considered with more care.

SuperDARN (Super Dual Auroral Radar Network) polar convection field plots for the event indicate that it is located in the morning sector of the polar cap, wherein the meridional component of the closing current is southward and the arc-associated electric field is located on the poleward edge. In this regime, the outflow of the cold ionospheric electrons creates a region of low conductivity on the poleward edge of the arc (Doe et al., 1995), leading to a "step-like" transition region in the ionospheric conductivity. Figure 6a shows EISCAT raw electron density profiles for an extended period of time surrounding this event; enhanced electron density indicates the period of time in which electron precipitation corresponding to the optical arc was within the ESR field of view. As expected a localized decrease in electron density, corresponding to the closing current, is observed between 20:50:30 and 20:50:40 UT, shortly before the arc enters the field of view. As a result, despite the background convection field having the correct orientation, it is not able to drive a strong enough Pedersen current to close the arc's FAC through the ionosphere; therefore an enhancement of the electric field is required (Aikio et al., 1993). In the upper E and F region ionosphere the ion gyrofrequency is approximately equal to the ion-neutral collision frequency, and strong electric field in this region will therefore drive a Pedersen current through the ionosphere, parallel to the electric field. Typical values of the convective electric field at auroral latitudes are a few mV/m, whereas some observations have described enhancements of up to 100 mV/m in the region of discrete auroral features (Aikio et al., 1993), often accompanied by enhanced ion or electron temperatures (Williams et al., 1990). However, the high-latitude electric field shows significant variability (Codrescu et al., 2000; Crowley & Hackert, 2001) and thus any spatial and temporal averaging of observations can lead to underestimates in the peak electric field magnitude. Lanchester et al. (1998) report electric field measurements during the passage of an arc system through an EISCAT radar beam at 3 s resolution. They observed a peak value of electric field strength of 600 mV/m ~10 km from and oriented in the direction of the main arc structure. Emphasis is placed on the importance of high-resolution optical observations, alongside radar measurements of the electric field, to interpret the variability and response to temporal changes in the arc unambiguously.

Equation (1) describes the rate of the energy dissipation into the neutral ionosphere in the form of frictional heating, or Joule heating. Since the ionospheric magnetic field can be assumed to be approximately constant ($\sim 5 \times 10^5$ nT) the main contributing factors to the heating rate are Pedersen conductivity ($\sigma_p(h)$), the electric field strength ($\mathbf{E}_\perp$) and the ionospheric neutral wind speed ($\mathbf{u}(h)$). This equation can be written in terms of the difference in velocity between ions and neutrals. Since ions in the upper E and F region ionosphere move according to the $\mathbf{E} \times \mathbf{B}$ drift, and thus substituting $\mathbf{E} = -\mathbf{v} \times \mathbf{B}$ into equation (1), we arrive at

$$Q_j(h) = \sigma_p(h)\left\{\left[\mathbf{u}(h) - \mathbf{v}(h)\right] \times \mathbf{B}\right\}^2 \quad (2)$$

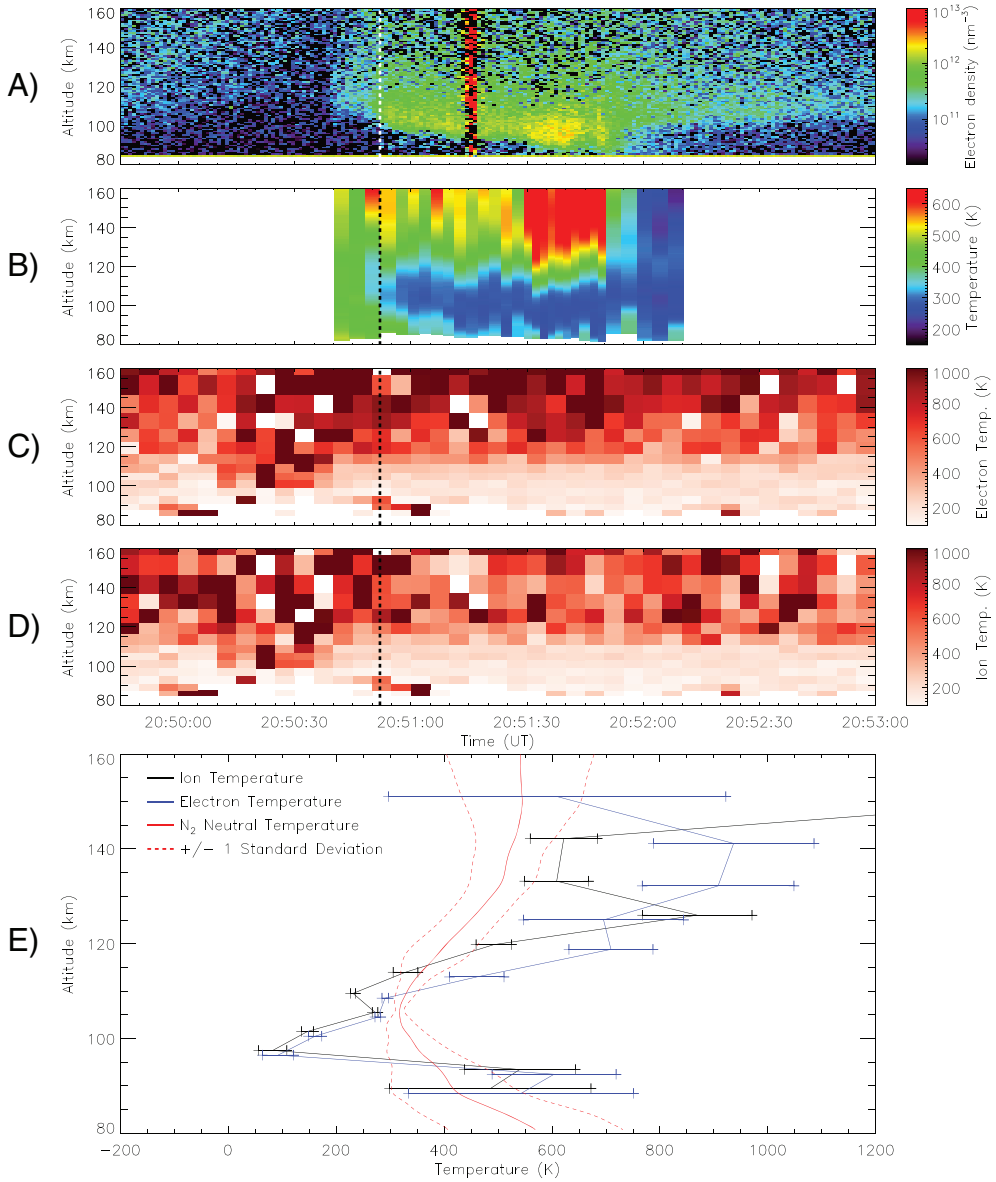

Figure 6. EISCAT Svalbard radar derived plasma parameters from 20:50:00 - 20:53:00 UT. A reduction in electron density immediately prior to the arrival of the arc in the radar beam, at 20:50:40 UT, is present in panel1. Panel 2 displays the measured N_2 neutral temperature profiles for the duration of the arc. Panels 3 & 4 show an asymmetric increase in electron and ion temperature, observed only on the poleward edge of the arc, as well as a smaller heating signature at low altitudes (90–100 km) associated with the arcs first entry into the ESR radar beam. The vertical dashed lines in the top four panels mark the time at which the electron and ion temperature profiles are plotted in panel 5. Ion an electron temperature profiles in panel 5 are displaced 0.5 km upward and downward, respectively, to assist readability.

where $\mathbf{v}(h)$ is the ionospheric ion velocity. During periods of intense auroral activity the Joule heating rate ($Q_j(h)$) is significantly enhanced by both the increased ionization, and therefore Pedersen conductivity, associated with particle precipitation and the accelerated ion velocity due to the large localized electric fields discussed above. We propose that the large observed increase in neutral temperature between 80 and 160 km, poleward of the arc, is caused by the transfer of energy from ionospheric ions to neutrals in the form of a large frictional heating term, being driven by the presence of an arc-associated electric field. Figures 6b–6d display a comparison between the measured N_2 neutral temperatures with the ESR-derived electron and ion temperatures, respectively. The electron and ion temperatures (Figures 6c and 6d) show a clear region of increased temperatures, between 20:50:10 and 20:50:40 UT, present at altitudes as low as 100 km, which

only appears on the poleward edge of the arc. This is in agreement with our results and is likely the lower limit of a large-altitude region over which the Joule heating is present. Previous studies have shown the effects of Joule heating on ion temperatures up to altitudes of 250 km and higher (Opgenoorth et al., 1990; Williams et al., 1990).

4.2. Arc-Associated Ohmic Heating

The second interesting feature present in the reported neutral temperature profiles is the localized heating (~50 K) observed at times over a narrow altitude range between ~90 and 110 km. This signature is present within the arc itself, rather than adjacent to it, and therefore we will refer to it as "arc-associated Ohmic heating." The temperatures in this altitude region, within the optical arc, are highest during the time window just after the bright edge of the arc has moved into the HiTIES slit. This can be seen in the top panel of Figure 4, as a green-shaded region between 20:50:48 and 20:50:59 UT, centered on ~95 km, and in the individual temperature profile in Figure 5b, where the temperature measured at this altitude shows a large positive increase below 100 km. Further to this, in Figures 6c and 6d, a signature of increased ion and electron temperatures, measured by ESR, can be seen at low altitudes (80–95 km) during the same time period. The highest magnitude ion and electron temperatures are seen at an altitude of 80–90 km between 20:51:00 and 20:51:05 UT. The N_2 neutral temperatures at this time do not display a similar signature; there is no significant N_2 volume emission at altitudes below 90 km (signified by the white shaded region), and consequently, we cannot produce accurate neutral temperatures in this range. However, in the 15 s preceding this, the enhanced ion and electron temperatures are present at higher altitudes, where there is more N_2 volume emission, and thus we are able to observe more clearly a corresponding increase in the N_2 neutral temperature. Individual ion and electron temperature profiles are plotted in the bottom panel for the time indicated with a vertical dashed line. Electron and ion temperature profiles show a clear spike in temperature below 95 km, a change of temperature that is significant in comparison to the errors associated with the measurements. This indicates that although this signature is near the floor of the ESR signal range, it is likely real. The corresponding N_2 neutral temperature profile is displayed in red.

Further heating signatures in the N_2 neutral temperature, between 80 and 100 km, are observed in the top panel of Figure 4 for the remainder of the event. These observed temperature changes are not as significant in magnitude, do not typically persist for extended periods of time, and are derived from a region of low volume emission and hence large uncertainty. In addition, they display no clear correlation with the ESR ion and electron temperatures. As a result of this, for the remainder of this discussion we will focus solely on the Ohmic heating observed at the poleward, leading edge of the arc.

The physical mechanism behind the arc-associated Ohmic heating is not as clear or well documented as the Joule heating discussed in the previous section. The majority of studies prior to this one have not reported a feature of this nature, particularly since it is seen in the neutral temperature. The timescale and magnitude of the heating is extremely fine, and therefore, it would most likely be averaged out or missed completely in observations with lower resolution. The signature occurs well within the *E* region ionosphere where ion-neutral collision rates strongly couple the motion of both species therefore inhibiting the formation of significant Pedersen currents. Zhu et al. (2001) presented results from a two-dimensional three-fluid model of the ionosphere-magnetosphere system. Along with a companion paper (Lanchester et al., 2001), they conducted an extensive study into the various sources of ionospheric ion and electron heating in order to explain optical and radar observations of a filamentary aurora event. Of particular interest is their treatment of electron heating sources, which they separate into two regimes: particle precipitation and Ohmic heating. They find that to account for observed changes in electron temperature, a large contribution from FAC associated Ohmic heating is needed. In the Zhu et al. (2001) model, the Ohmic heating effects are found in a narrow current sheet located at sharp precipitation boundaries, such as those observed in our event and others (Arnoldy, 1974). The Ohmic heating term is proportional to $\eta\mathbf{j}$, where η is the resistivity and $\mathbf{j}$ is the current density. The model shows an approximately constant current density and an exponential increase in resistivity with decreasing altitude; as a result, it would be expected that the maximum Ohmic heating rate is at the bottom of the FAC sheet (Zhu et al., 2001 Figure 7b.). Furthermore, since the electron-neutral collision frequency exponentially increases with decreasing altitude, the electron cooling via neutral collisions also increases, and the characteristic timescale to achieve a steady state between the two is short. While the neutral temperature would not respond significantly to the electron temperature fluctuations, we could expect that given a strong enough FAC, the corresponding signature in neutral temperatures, if any, would be located in this region.

The ESR ion and electron temperature data (Figures 6c and 6d) show three distinct time intervals containing enhanced temperatures (>∼500 K) at the expected altitude range: (X) between 20:49:55 and 20:50:10 UT; (Y) between 20:50:45 and 20:51:05 UT; and (Z) between 20:52:50 and 20:52:55 UT. Only the second of these intervals (Y) occurred during a period of N_2 emission, allowing for corresponding N_2 neutral temperatures to be determined and is believed to be due to Ohmic heating effects arising from an intense, narrow upward FAC sheet. The ASK video for this time shows a period of dynamical features, consisting of strong shear flows and multiple bright curls propagating along the poleward arc boundary from west to east. Intervals X and Z are thought to be a similar phenomena. X occurs during a period of negligible auroral emission and therefore has no associated upward current; instead, it is believed that a companion downward FAC sheet, linked with Y and further ensuring ionospheric current continuity, is responsible for the Ohmic heating in this interval. Z occurs approximately 10 s after the end of N_2 neutral temperature observations when the N_2 brightness is too low for any appreciable results. The ASK video for this time shows an extremely faint set of curls moving through the magnetic zenith, linking this signature to an upward FAC sheet that is present either on the trailing edge of the previous arc structure or as a stand-alone formation.

Our results suggest that certain auroral features such as curls, shear flows or regions where there is a sharp boundary in emission brightness are likely associated with narrow and intense current sheets, which can deposit energy into the lower *E* region of the neutral atmosphere via Ohmic heating processes.

5. Conclusions

We have provided direct observational evidence of the large-scale electrodynamical system responsible for the formation of an auroral arc and of small-scale FAC sheets embedded within the arc, associated with its dynamical structure. The thermosphere is an important energy sink for magnetosphere-ionospheric interactions and observations of that mechanism on local scales are extremely important for quantifying the total global response. The neutral temperature has shown a rapid, and significant, response to the presence of electric currents on time scales of the order of seconds and spatial scales smaller than 10 km. First results from a new observational technique provide high-resolution measurements of the evolution of the atmospheric neutral temperature profile, associated with a high-energy auroral event over Svalbard. The process involves simultaneous observations from two optical instruments, ASK and the HiTIES as well as electron density measurements from the ESR. By fitting a library of synthetic N_2 emission spectra to observed spectra, taken from HiTIES, we are able to estimate the shape of the neutral temperature profile for a series of time steps, covering the auroral event. The key results of this study are summarized below.

Optical observations begin at 20:50:40 UT, just after a decrease in ESR electron density (Figure 6a) which we have associated with a downward current of upward flowing cold ionospheric electrons (section 4.1). For the first 4 s (20:50:40–20:50:44 UT) of observation, the associated neutral temperature profile shows a significant increase in temperature at altitudes as low as 80 km, generated by ion-neutral frictional heating as a result of a strong arc-perpendicular electric field and consequent meridional Pedersen currents. These Pedersen currents act as a current closure mechanism linking the downward current with the upward current associated with the optical arc.

As the arc moves in to the field of view over the next 8 s (20:50:44–20:50:52 UT), bringing with it a region of strong upward FAC, the associated temperature profile rapidly evolves. Neutral temperatures between 100 and 130 km decrease by ∼100 K and a small-scale increase of ∼50 K is seen between 90 and 100 km, coincident with simultaneous ESR ion and electron temperature measurements. The ion temperature, and hence associated neutral temperature, should decrease to background levels because the fast ion flow is associated with the strong electric fields outside the optical arc. The electron temperature at this time is significantly affected by Ohmic dissipative heating on the leading edge of the arc. Due to collision rates and resistivity varying with altitude, the largest response in the neutral temperature associated with this electron heating is expected to be concentrated at the lower end of the FAC sheet, as is observed (section 4.2).

The arc then remains in the field of view for ∼60 s following its first entry, and the corresponding temperature profiles show relatively small variation with time. Ohmic heating at the same altitudes as previous signatures (90–100 km) is present, potentially caused by filamentary current systems embedded in the arc itself, although no accompanying ESR ion or electron temperatures variations are observed. When the arc

exits the field of view, the temperature profiles measured on its equatorward edge transition to a significantly cooler regime in comparison to those observed on the poleward edge.

Acknowledgments
This work was supported by the Natural Environmental Research Council (Grant NE/R009783/1 and NE/N004051/1). EISCAT is an international association supported by research organizations in China (CRIRIP), Finland (SA), France (CNRS, until 2006), Germany (DFG), Japan (NIPR and STEL), Norway (NFR), Sweden (VR), and the United Kingdom (STFC and NERC). Radar data are available from the CEDAR Madrigal database and can be downloaded from https://www.eiscat.se/madrigal/cgi-bin/madExperiment.cgi?exp=2017/lyr/27jan17&displayLevel=0 (Ingemar Häggström, EISCAT Scientific Association, 2017). Supporting information including ASK keograms, videos of the 2 min interval observed in ASK, and the HiTIES emission spectra at half-second resolution are available at this website (http://doi.org/10.5258/SOTON/D1056).

References

Aikio, A., Opgenoorth, H., & Persson, M. (1993). Ground-based measurements of an arc-associated electric field. *Journal of Atmospheric and Terrestrial Physics*, *55*(4–5), 797–808.

Arnoldy, R. (1974). Auroral particle precipitation and Birkeland currents. *Reviews of Geophysics*, *12*(2), 217–231.

Ashrafi, M. (2007). ASK: Auroral structure and kinetics in action. *Astronomy & Geophysics*, *48*(4), 4–35.

Boström, R. (1964). A model of the auroral electrojets. *Journal of Geophysical Research*, *69*(23), 4983–4999.

Chadney, J. M., Whiter, D. K., & Lanchester, B. S. (2017). Effect of water vapour absorption on hydroxyl temperatures measured from Svalbard. *Annales Geophysicae*, *35*, 481–491.

Chun, F. K., Knipp, D. J., McHarg, M. G., Lacey, J. R., Lu, G., & Emery, B. A. (2002). Joule heating patterns as a function of polar cap index. *Journal of Geophysical Research*, *107*(A7), 1119. https://doi.org/10.1029/2001JA000246

Chun, F. K., Knipp, D. J., McHarg, M. G., Lu, G., Emery, B. A., Vennerstrøm, S., & Troshichev, O. A. (1999). Polar cap index as a proxy for hemispheric Joule heating. *Geophysical Research Letters*, *26*(8), 1101–1104.

Codrescu, M., Fuller-Rowell, T., & Foster, J. (1995). On the importance of E-field variability for Joule heating in the high-latitude thermosphere. *Geophysical Research Letters*, *22*(17), 2393–2396.

Codrescu, M., Fuller-Rowell, T., Foster, J., Holt, J., & Cariglia, S. (2000). Electric field variability associated with the Millstone Hill electric field model. *Journal of Geophysical Research*, *105*, 5265–5273. https://doi.org/10.1029/1999JA900463

Crowley, G., & Hackert, C. L. (2001). Quantification of high latitude electric field variability. *Geophysical Research Letters*, *28*, 2783–2786. https://doi.org/10.1029/2000GL012624

Dahlgren, H., Ivchenko, N., Sullivan, J., Lanchester, B., Marklund, G., & Whiter, D. (2008). Morphology and dynamics of aurora at fine scale: First results for the ASK instrument. *Annales Geophysicae*, *26*(5), 1041–1048.

Doe, R., Vickrey, J., & Mendillo, M. (1995). Electrodynamic model for the formation of auroral ionospheric cavities. *Journal of Geophysical Research*, *100*(A6), 9683–9696.

Fujii, R., Nozawa, S., Buchert, S. C., & Brekke, A. (1999). Statistical characteristics of electromagnetic energy transfer between the magnetosphere, the ionosphere, and the thermosphere. *Journal of Geophysical Research*, *104*(A2), 2357–2365.

Han, D.-S., Xu, T., Jin, Y., Oksavik, K., Chen, X.-C., Liu, J.-J., et al. (2019). Observational evidence for throat aurora being associated with magnetopause reconnection. *Geophysical Research Letters*, *46*, 7113–7120. https://doi.org/10.1029/2019gl083593

Henriksen, K., Veseth, L., Deehr, C. S., & Smith, R. W. (1987). Neutral temperatures and emission height changes in an *E*-region aurora. *Planetary and space science*, *35*(10), 1317–1321.

Iijima, T., & Potemra, T. A (1976). The amplitude distribution of field-aligned currents at northern high latitudes observed by Triad. *Journal of Geophysical Research*, *81*(13), 2165–2174.

Iijima, T., & Potemra, T. A. (1978). Large-scale characteristics of field-aligned currents associated with substorms. *Journal of Geophysical Research*, *83*(A2), 599–615.

Jokiaho, O., Lanchester, B., Ivchenko, N., Daniell, G., Miller, L., & Lummerzheim, D. (2008). Rotational temperature of $N_{2+}(0, 2)$ ions from spectrographic measurements used to infer the energy of precipitation in different auroral forms and compared with radar measurements. *Annales Geophysicae*, *26*(4), 853–866.

Kaila, K (1989). Determination of the energy of auroral electrons by the measurements of the emission ratio and altitude of aurorae. *Planetary and Space Science*, *37*(3), 341–349.

Kiene, A., Bristow, W., Conde, M., & Hampton, D. (2019). High-resolution local measurements of *F* region ion temperatures and Joule heating rates using SuperDARN and ground-based optics. *Journal of Geophysical Research: Space Physics*, *124*, 557–572. https://doi.org/10.1029/2018ja025997

Kosch, M. J., & Nielsen, E. (1995). Coherent radar estimates of average high-latitude ionospheric Joule heating. *Journal of Geophysical Research*, *100*(A7), 12,201–12,215.

Kosch, M., Yiu, I., Anderson, C., Tsuda, T., Ogawa, Y., Nozawa, S., et al. (2011). Mesoscale observations of Joule heating near an auroral arc and ion-neutral collision frequency in the polar cap *E* region. *Journal of Geophysical Research*, *116*, A05321. https://doi.org/10.1029/2010JA016015

Kurihara, J., Abe, T., Oyama, K.-I., Griffin, E., Kosch, M., Aruliah, A., et al. (2006). Observations of the lower thermospheric neutral temperature and density in the DELTA campaign. *Earth, planets and space*, *58*(9), 1123–1130.

Kurihara, J., Oyama, S., Nozawa, S., Tsuda, T., Fujii, R., Ogawa, Y., et al. (2009). Temperature enhancements and vertical winds in the lower thermosphere associated with auroral heating during the DELTA campaign. *Journal of Geophysical Research*, *114*, A12306. https://doi.org/10.1029/2009JA014392

Lanchester, B., Ashrafi, M., & Ivchenko, N. (2009). Simultaneous imaging of aurora on small scale in OI (777.4 nm) and N_2 1P to estimate energy and flux of precipitation. *Annales Geophysicae*, *27*(7), 2881–2891.

Lanchester, B., Kaila, K., & McCrea, I. (1996). Relationship between large horizontal electric fields and auroral arc elements. *Journal of Geophysical Research*, *101*(A3), 5075–5084.

Lanchester, B., Palmer, J., Rees, M., Lummerzheim, D., Kaila, K., & Turunen, T. (1994). Energy flux and characteristic energy of an elemental auroral structure. *Geophysical Research Letters*, *21*(25), 2789–2792.

Lanchester, B., Rees, M., Lummerzheim, D., Otto, A., Sedgemore-Schulthess, K, Zhu, H., & McCrea, I. (2001). Ohmic heating as evidence for strong field-aligned currents in filamentary aurora. *Journal of Geophysical Research*, *106*, 1785–1794.

Lanchester, B., Rees, M., Sedgemore, K., Palmer, J., Frey, H., & Kaila, K. (1998). Ionospheric response to variable electric fields in small-scale auroral structures. *Annales Geophysicae*, *16*(10), 1343–1354.

Lühr, H., & Warnecke, J. (1994). Fine structure of field-aligned current sheets deduced from spacecraft and ground-based observations: Initial FREJA results. *Geophysical Research Letters*, *21*(17), 1883–1886.

Lummerzheim, D., & Lilensten, J. (1994). Electron transport and energy degradation in the ionosphere: Evaluation of the numerical solution, comparison with laboratory experiments and auroral observations. *Annales geophysicae*, *12*(10), 1039–1051.

Maeda, S., Nozawa, S., Ogawa, Y., & Fujiwara, H. (2005). Comparative study of the high-latitude *E* region ion and neutral temperatures in the polar cap and the auroral region derived from the EISCAT radar observations. *Journal of Geophysical Research*, *110*, A08301. https://doi.org/10.1029/2004JA010893

Marghitu, O. (2012). Auroral arc electrodynamics: Review and outlook. *Auroral Phenomenology and Magnetospheric Processes: Earth And Other Planets*, *197*, 143–158.

Marklund, G. (1984). Auroral arc classification scheme based on the observed arc-associated electric field pattern. *Planetary and Space Science*, *32*(2), 193–211.

Marklund, G., Sandahl, I., & Opgenoorth, H. (1982). A study of the dynamics of a discrete auroral arc. *Planetary and Space Science*, *30*(2), 179–197.

Nozawa, S., Ogawa, Y., Brekke, A., Tsuda, T., Hall, C. M., Miyaoka, H., et al. (2006). Eiscat observational results during the delta campaign. *Earth, Planets and Space*, *58*(9), 1183–1191.

Opgenoorth, H., Hägström, I., Williams, P., & Jones, G. (1990). Regions of strongly enhanced perpendicular electric fields adjacent to auroral arcs. *Journal of Atmospheric and Terrestrial Physics*, *52*(6-8), 449–458.

Østgaard, N., Germany, G., Stadsnes, J., & Vondrak, R. (2002). Energy analysis of substorms based on remote sensing techniques, solar wind measurements, and geomagnetic indices. *Journal of Geophysical Research*, *107*(A9), 1233. https://doi.org/10.1029/2001JA002002

Palmer, J. R. (1995). Plasma density variations in aurora (Unpublished doctoral dissertation), University of Southampton, University Road, Southampton.

Partamies, N., Syrjäsuo, M., Donovan, E., Connors, M., Charrois, D., Knudsen, D., & Kryzanowsky, Z. (2010). Observations of the auroral width spectrum at kilometre-scale size. *Annales Geophysicae*, *28*(3), 711–718.

Picone, J., Hedin, A., Drob, D. P., & Aikin, A. (2002). NRLMSISE-00 empirical model of the atmosphere: Statistical comparisons and scientific issues. *Journal of Geophysical Research*, *107*(A12), 1468. https://doi.org/10.1029/2002JA009430

Rodger, A., Wells, G., Moffett, R., & Bailey, G. (2001). The variability of Joule heating, and its effects on the ionosphere and thermosphere. *Annales Geophysicae*, *19*(7), 773–781.

Roux, F., & Michaud, F. (1990). Investigation of the rovibrational levels of the $B^3\Pi_g$ state of $^{14}N_2$ molecule above the dissociation limit $N(^4S)+ N(^4)$ by Fourier transform spectrometry. *Canadian Journal of Physics*, *68*(11), 1257–1261.

Sandahl, I., Sergienko, T., & Brändström, U. (2008). Fine structure of optical aurora. *Journal of Atmospheric and Solar-Terrestrial Physics*, *70*(18), 2275–2292.

Sharber, J., Frahm, R., Link, R., Crowley, G., Winningham, J., Gaines, E., et al. (1998). UARS particle environment monitor observations during the November 1993 storm: Auroral morphology, spectral characterization, and energy deposition. *Journal of Geophysical Research*, *103*(A11), 26,307–26,322.

Stasiewicz, K., & Potemra, T. (1998). Multiscale current structures observed by Freja. *Journal of Geophysical Research*, *103*(A3), 4315–4325.

Timofeev, E., Vallinkoski, M., Kozelova, T., Yahnin, A., & Pellinen, R. (1987). Systematics of arc-associated electric-fields and currents as inferred from radar backscatter measurements. *Journal of Geophysics*, *61*(2), 122–137.

Tsunoda, R., Presnell, R., & Potemra, T. (1976). The spatial relationship between the evening radar aurora and field-aligned currents. *Journal of Geophysical Research*, *81*(22), 3791–3802.

Whiter, D., Lanchester, B., Gustavsson, B., Jallo, N., Jokiaho, O., Ivchenko, N., & Dahlgren, H. (2014). Relative brightness of the O^+ (^2D-^2P) doublets in low-energy aurorae. *The Astrophysical Journal*, *797*(1), 64.

Williams, P., Jones, G., Jones, B., Opgenoorth, H., & Hägström, I. (1990). High-resolution measurements of magnetospheric electric fields. *Journal of Atmospheric and Terrestrial Physics*, *52*(6-8), 439–448.

Wu, J., Knudsen, D., Gillies, D., Donovan, E., & Burchill, J. (2017). Swarm observation of field-aligned currents associated with multiple auroral arc systems. *Journal of Geophysical Research: Space Physics*, *122*, 10,145–10,156. https://doi.org/10.1002/2017JA024439

Zhu, H., Otto, A., Lummerzheim, D., Rees, M., & Lanchester, B. (2001). Ionosphere-magnetosphere simulation of small-scale structure and dynamics. *Journal of Geophysical Research*, *106*, 1795–1806. https://doi.org/10.1029/1999JA000291